ASC Crystal Growth and Design Manuscript Draft

Title: Particle Breakage Kinetics and Mechanisms in Attrition-Enhanced Deracemization

Authors: Christos Xiouras[†], Antonios A. Fytopoulos[†,□], Joop H. Ter Horst[‡], Andreas G. Boudouvis[□], Tom Van Gerven[†] and Georgios D. Stefanidis[†*]

† Process Engineering for Sustainable Systems (ProcESS), Department of Chemical Engineering KU Leuven, Celestijnenlaan 200F, 3001 Leuven, Belgium

‡ EPSRC Centre for Innovative Manufacturing in Continuous Manufacturing and Crystallisation (CMAC), Strathclyde Institute of Pharmacy and Biomedical Sciences (SIPBS), Technology and Innovation Centre, University of Strathclyde, 99 George Street, Glasgow G1 1RD, U.K.

□ Process Analysis and Plant Design, School of Chemical Engineering NTUA, 9 Heroon Polytechniou, Zografou, 15780 Athens, Greece

[*]Correspondence to: Georgios D. Stefanidis

Tel**:** +32(0)16321007

E-mail: Georgios.Stefanidis@cit.kuleuven.be

Type of Manuscript: Article

Keywords: deracemization; Viedma ripening; particle breakage; bead grinding; ultrasound grinding; abrasion; fracture; sodium chlorate

Abstract: In this study, we report on experiments designed to deconvolute the particle breakage kinetics and mechanism from the parallel phenomena (growth-dissolution, agglomeration) in attrition-enhanced deracemization processes. Through such experiments, we derived the specific breakage rates and cumulative breakage distribution functions for three grinding methods typically used in deracemization experiments: a) bead grinding, b) ultrasound grinding and c) the combination of bead and ultrasound grinding. Subsequently, we tested these methods on their ability to induce deracemization. We show that in the conventional bead grinding process, breakage occurs mostly by fracture. This results in slow deracemization rates due to the delayed formation of submicron particles that are essential to the process. Conversely, ultrasound grinding very efficiently breaks particles by abrasion. This leads to fast generation of an abundance of submicron fragments resulting in fast deracemization. However, using ultrasound, large crystals fracture rates are an order of magnitude lower than those using bead grinding, which results in an insufficient size decrease of the large counter enantiomer crystals and eventually to incomplete deracemization. Remarkably, the simultaneous application of bead and ultrasound grinding leads, due to synergistic effects of both fracture and abrasion, to 2-fold higher total deracemization rates compared to bead grinding alone. The present work offers new insights into the key role of particle breakage in attrition-enhanced deracemization, together with a basis for decoupling the individual phenomena involved in the process.

Particle Breakage Kinetics and Mechanisms in Attrition-Enhanced Deracemization

Christos Xiouras[†], *Antonios A. Fytopoulos*[†,□], *Joop H. Ter Horst*[‡], *Andreas G. Boudouvis*[□], *Tom Van Gerven*[†] *and Georgios D. Stefanidis*[†,□]

† Process Engineering for Sustainable Systems (ProcESS), Department of Chemical Engineering KU Leuven, Celestijnenlaan 200F, 3001 Leuven, Belgium

‡ EPSRC Centre for Innovative Manufacturing in Continuous Manufacturing and Crystallisation (CMAC), Strathclyde Institute of Pharmacy and Biomedical Sciences (SIPBS), Technology and Innovation Centre, University of Strathclyde, 99 George Street, Glascow G1 1RD, U.K.

□ Process Analysis and Plant Design, School of Chemical Engineering NTUA, 9 Heroon Polytechniou, Zografou, 15780 Athens, Greece

[*]Correspondence to: Georgios D. Stefanidis

Tel: +32(0)16321007, Email: Georgios.Stefanidis@cit.kuleuven.be

KEYWORDS: particle breakage; deracemization; Viedma ripening; sodium chlorate; ultrasound; abrasion; fracture; attrition

ABSTRACT

In this study, we report on experiments designed to deconvolute the particle breakage kinetics and mechanism from the parallel phenomena (growth-dissolution, agglomeration) in attrition-

enhanced deracemization processes. Through such experiments, we derived the specific breakage rates and cumulative breakage distribution functions for three grinding methods typically used in deracemization experiments: a) bead grinding, b) ultrasound grinding and c) the combination of bead and ultrasound grinding. Subsequently, we tested these methods on their ability to induce deracemization. We show that in the conventional bead grinding process, breakage occurs mostly by fracture. This results in slow deracemization rates due to the delayed formation of submicron particles that are essential to the process. Conversely, ultrasound grinding very efficiently breaks particles by abrasion. This leads to fast generation of an abundance of submicron fragments resulting in fast deracemization. However, using ultrasound, large crystals fracture rates are an order of magnitude lower than those using bead grinding, which results in an insufficient size decrease of the large counter enantiomer crystals and eventually to incomplete deracemization. Remarkably, the simultaneous application of bead and ultrasound grinding leads, due to synergistic effects of both fracture and abrasion, to 2-fold higher total deracemization rates compared to bead grinding alone. The present work offers new insights into the key role of particle breakage in attrition-enhanced deracemization, together with a basis for decoupling the individual phenomena involved in the process.

1. INTRODUCTION

In 2005, Viedma [1] reported on a remarkable and non-classical crystallization phenomenon wherein a racemic population of conglomerate crystals of the achiral $NaClO_3$ converts to a single chirality by simply breaking the particles in contact with their saturated solution (*e.g.* stirring the suspension in the presence of grinding media). A few years later, Noorduin et al. [2] successfully developed the equivalent process for intrinsically chiral molecules that undergo racemization and

form conglomerate crystals, establishing the attrition-enhanced deracemization or Viedma ripening process as a feasible means to obtain enantiopure pharmaceutical precursors in quantitative yields [3–5]. Since the seminal studies of Viedma and Noorduin, several achiral [6–8] and chiral [9–16] compounds have been successfully deracemized and many intriguing variations of the process have appeared, such as temperature cycling-enhanced deracemization [17–19], combination of Viedma ripening with reactions [20,21] or crystal transformations [22–24] or the concomitant use of Viedma ripening with chiral additives [25,26].

Meanwhile, current research pursues a better understanding of the complex physical and chemical mechanisms underlying the phenomenon. According to the present scientific consensus, the mechanisms under which Viedma ripening occurs can be rationalized by the effects of: a) racemization (only for intrinsically chiral compounds), b) particle breakage, c) growth-dissolution subject to the size dependence of solubility and d) chirally selective agglomeration [1,27–31]. Breakage keeps generating fragments of both enantiomer crystals, small enough to dissolve, each having the same chirality as the parent crystal. Under these conditions, it is believed that the enantiomer in (slight) initial excess would have more of its crystals and fragments in the suspension and will therefore experience a faster overall agglomeration rate than its antipode. As a result, the fragments of the excess enantiomer are effectively "saved" from dissolution, while the minor enantiomer fragments mostly dissolve and racemize or lose chiral identity providing monomers for further growth of the major enantiomer. The actual size of fragments required for fast deracemization is for the moment unclear, but a consideration of the Gibbs-Thomson equation (see Supporting information) shows that, for most compounds, only fragments in the range of 1 μm and below would exhibit substantially higher solubility compared to the larger crystals, while particles larger than about 10 μm are not expected to differ

considerably in their solubility and would be rather stable. Submicron fragments are also influenced more by agglomeration too, as agglomeration also depends on the particle size and number, with particles larger than about 10 μm not being expected to agglomerate significantly at low supersaturations [32].

In experimental investigations of Viedma ripening, substantial differences have been observed in the deracemization rate, when the nature of the breakage and its parameters are altered [1]. However, the influence of the various grinding mechanisms and breakage kinetics remain unexplored and the words breakage, abrasion, attrition and fracture are often used interchangeably to describe the fragmentation process, even when the breakage sources applied and/or their operating conditions differ significantly. In addition, various studies have reported deracemization using novel breakage sources, such as ultrasound [33] either in the presence [4,31,34,35] or absence [36,37] of grinding media. In these studies, several intriguing and/or contradicting phenomena have been observed, such as enhancement of the deracemization rate using ultrasound with beads [14,34] or without beads [36,37], and incomplete deracemization [36]. The mechanisms of ultrasound breakage are expected to differ substantially compared to the grinding mechanisms in stirred media mills. While bead grinding leads to particle breakage through impact forces between the particles and the grinding media, ultrasound is believed to result in particle breakage through the phenomenon of acoustic cavitation and in particular the implosive collapse of cavitation bubbles followed by shock-waves, liquid jets and inter-particle collisions, all of which result in mechanical stress to the particles [38].

Depending on the mechanical properties of the particles (hardness, elasticity) and the nature and intensity of the applied stress, particle breakage generally occurs either by fracture or abrasion or a combination of the two mechanisms [39]. Fracture is defined as the splitting of a mother particle

resulting in its complete disappearance and the generation of several smaller fragments over a broad distribution of sizes. Fracture occurs usually in response to rapid stress applied on the particle, such as impact force. In contrast, abrasion is defined as the mechanism of size reduction by which very fine fragments are chipped off from the edges and surface of the mother particle, while the mother particle undergoes only a small size reduction. Abrasion usually arises due to the application of local low-intensity stress on a particle. In a typical wet-grinding process, the dominant fragmentation mechanisms can be identified by measuring the particle size distribution (PSD) in time. However, to do so in a Viedma ripening process, one would have to experimentally decouple all parallel phenomena that affect the PSD, *i.e.* growth/dissolution and agglomeration. This challenge can be alleviated by working with nonsolvents to characterize the breakage alone using different types of grinding and operating conditions, in the absence of other phenomena, and then transfer the results to actual Viedma ripening experiments.

In this study, we aim to deconvolute the different breakage mechanisms in attrition-enhanced deracemization processes. Through particle breakage experiments in nonsolvent for the model compound $NaClO_3$, we derive and compare the breakage kinetics and relevant breakage mechanisms for three grinding methods commonly used in attrition-enhanced deracemization experiments: a) conventional bead grinding, b) ultrasound grinding and c) the combination of bead and ultrasound grinding. Subsequently, the grinding methods are tested in actual deracemization experiments. This work provides further insights into the effect of particle breakage in Viedma ripening, together with a basis for decoupling the individual phenomena involved in the process.

2. KINETIC MODEL FOR GRINDING

Regardless of the type of grinding employed, the evolution of the PSD in batch fragmentation processes is often described sufficiently by the following set of differential equations that define the mass balances in each of n discrete particle size classes [43]:

$$\frac{dm_i(t)}{dt} = -S_i m_i(t) + \sum_{j=1}^{i-1} S_j b_{i,j}\, m_j(t) \qquad (1)$$

$$i = 1, 2, 3, \ldots n$$

where t is the grinding time, $m_i(t)$ is the mass fraction (%) of particles in size class i (where i=1 corresponds to the coarsest size class), S_i is the breakage rate for particles in size class i and $b_{i,j}$ is the breakage distribution function, *i.e.* the mass fraction of particles from the jth size class that are broken to end up in size class i. Consequently, the first term on the right hand side of Eq. 1 describes the disappearance rate of particles in size class i due to breakage, while the second term describes the generation rate of particles in size class i due to the collective breakage of particles in all larger size classes.

Writing the exact equivalent of Eq. 1 in the cumulative form gives:

$$\frac{dR_i(t)}{dt} = -S_i R_i(t) + \sum_{j=1}^{i-1} (S_{j+1} B_{i,j+1} - S_j B_{i,j}) R_j(t) \qquad (2)$$

$$i = 1, 2, 3, \ldots n$$

where $R_i(t) = \sum_{j=1}^{i} m_j(t)$ is the cumulative oversize mass fraction (%), *i.e.* the mass fraction of all particles larger than the lower size bound of the ith size class (x_i) and $B_{i,j} = \sum_{k=i+1}^{n} b_{k,j}$ is the cumulative breakage distribution function, which represents the probability of fragments formed by breakage of particles in size class j to have a size less than x_i.

In a typical grinding process, the values of the $B_{i,j}$ and S_i functions are usually unknown, but they can be estimated from experimental PSD measurements data by solving Eq. 2 for any given set of size classes. Kapur [44] has shown that the solutions of Eq. 2 can be approximated for every size class i as a power series expansion in time:

$$\frac{R_i(t)}{R_i(0)} = \exp\left[\sum_{k=1}^{p} K_i^{(k)} \frac{t^k}{k!}\right] \tag{3}$$

Where $R_i(0)$ is the cumulative oversize mass fraction in size class i in the beginning of the grinding process and $K_i^{(k)}$ are the coefficients of the power series in the brackets, which have been shown [44] to be functions of $B_{i,j}$ and S_i. For short grinding times ($T < 95\%$), Eq. 3 can be approximated by keeping only the first term of the power series, while still maintaining a sufficient degree of accuracy [45]:

$$\frac{R_i(t)}{R_i(0)} \approx \exp\left[K_i^{(1)} t\right] \tag{4}$$

where T is the dimensionless grinding time and is defined as the percentage of particles broken out of each size class [46]:

$$T = \left[1 - exp\ (K_i^{(1)} t)\right] 100\% \tag{5}$$

Consequently, by experimentally measuring $R_i(t)$ and then plotting $\ln\left(\frac{R_i(t)}{R_i(0)}\right)$ versus t, $K_i^{(1)}$ can be obtained for any size class i and can subsequently be used to derive the approximate specific breakage rate S_i and cumulative breakage distribution functions $B_{i,j}$ according to [45,47–49]:

$$S_i = -K_i^{(1)} \tag{6}$$

$$B_{i,j} = \frac{K_i^{(1)}}{K_j^{(1)}} \tag{7}$$

Typically, the form of S_i and $B_{i,j}$ functions depends on the physical processes leading to breakage. While S_i characterizes the kinetics of the breakage process itself, $B_{i,j}$ characterizes the breakage event (average size distribution resulting from the breakage of a single particle) and it is indicative of the breakage mechanism [50]. For instance, a steep decrease in $B_{i,j}$ with decreasing particle size would indicate that particles are more likely to be broken to several larger fragments (fracture), while a more gradual decrease indicates that the probability of finer particle generation is high (abrasion). Menacho [51] derived the theoretical curves of $B_{i,j}$ against the relative particle size: $B_{i,j} = f\left(\frac{x_i}{x_j}\right)$, for the limiting cases of pure abrasion or fracture, shown in Figure 1. Thus, if the shape of the $B_{i,j}$ function is known or derived experimentally, a comparison with Figure 1 allows for the qualitative determination of the relative dominance of abrasion versus fracture in a grinding process. For most grinding processes, the curve is expected to lie between two extreme curves, shown in Figure 1, indicating that the grinding mechanism is, in most cases, a combination of both abrasion and fracture. The approach described in this Section will be used to derive the S_i and $B_{i,j}$ functions in order to identify the relevant breakage mechanisms and to compare the impact of the different modes of grinding on the deracemization process.

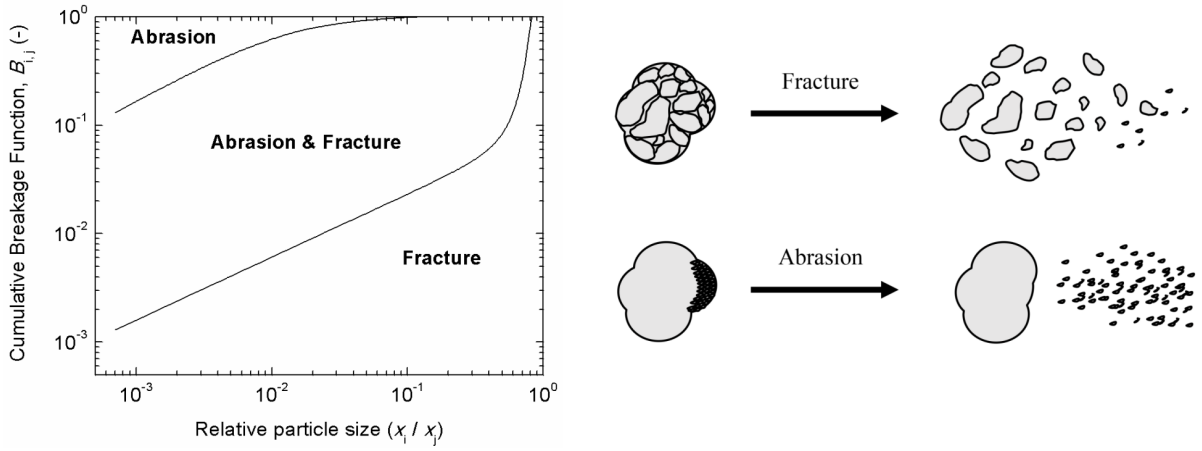

Figure 1. Left: Cumulative Breakage functions ($B_{i,j}$) versus relative particle size $\left(x_i/x_j\right)$ curves obtained for different breakage mechanisms for the ith and jth size classes [51]. Right: Schematic representation of the possible breakage mechanisms.

3. EXPERIMENTAL SECTION

3.1 Experimental setup for breakage and deracemization experiments

Figure 2 shows the experimental setup used in this study, which consists of a jacketed cylindrical crystallizer vessel, to which an ultrasound transducer is clamped at the bottom to allow proper sealing of the vessel. The internal suspension temperature was controlled at 22 °C by a Julabo thermostatic bath equipped with a Pt-100 temperature probe and the suspension was mixed by a Cole Parmer ultra-compact mixer using a two-bladed axial flow impeller (Ø 30 mm) at 800 rpm to avoid sedimentation of the particles. The absence of breakage due to mixing alone was confirmed by separate experiments, using only the mixer (Supporting Information).

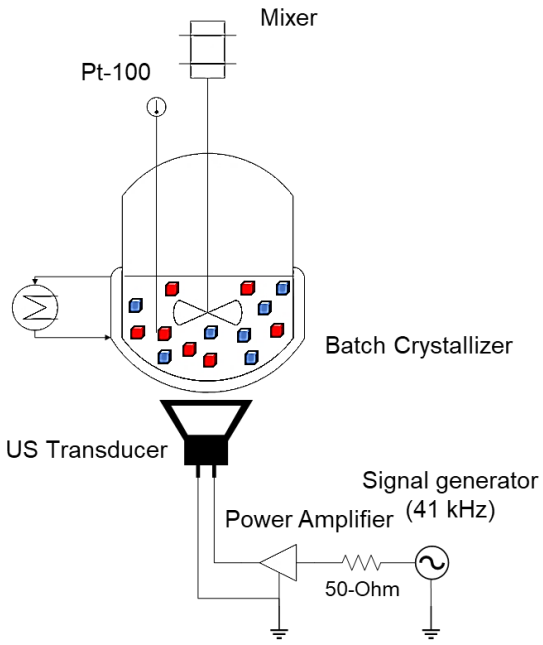

Figure 2. Experimental setup used for all breakage and deracemization experiments

3.2 Breakage experiments

All $NaClO_3$ breakage experiments were conducted in hexane, in which $NaClO_3$ is insoluble. From a stock solution of hexane (VWR) containing 1.5 wt% of lecithin, 100 mL were transferred into the crystallizer vessel. Lecithin was used as a surfactant to allow appropriate dispersion of the $NaClO_3$ particles. Subsequently, stirring (800 rpm), ultrasound at 41 kHz/30W (absorbed electrical power) and/or 40 g of glass beads (Ø 3 mm) were introduced. Finally, 20 g of $NaClO_3$ crystals (Sigma Aldrich, 99%, as received) were added in the vessel to start the breakage experiments. During the breakage process, suspension samples of approximately 4 mL were taken and were immediately transferred into the sample wet dispersion unit of a Malvern 3000 Mastersizer laser diffractometer containing 400 mL of 1.5 wt% lecithin in hexane and PSD measurements were immediately recorded (lower detection limit ~ 0.01 μm). The shape and

morphology of the particles was analyzed using a Philips XL 30 FEG scanning electron microscope.

3.3 Deracemization experiments

In all deracemization experiments, 100 mL of saturated aqueous $NaClO_3$ solution at 22 °C were transferred into the crystallizer vessel and stirring (800 rpm), ultrasound (41 kHz, 30 W) and/or 40 g (Ø 3 mm) of glass beads were introduced. Next, 20 g of $NaClO_3$ (Sigma Aldrich, 99%, as received) were added in the vessel to start the deracemization experiments. Suspension samples of approximately 2 mL were taken regularly, filtered over a P5 glass filter, washed by 2 mL of cold acetone to remove adhering solution and dried overnight in an oven set at 40 °C. The resulting crystals were analyzed for the determination of the solid phase enantiomeric excess.

Measurement of the solid-phase enantiomeric excess (ε) by solid-state Circular Dichroism (CD)

The solid phase ε of the crystals was measured by a similar technique, as reported elsewhere [7]. The solid samples were prepared as Nujol mulls, by grinding 0.1 g of the $NaClO_3$ crystals in mortar and pestle in Nujol mineral oil (10 w.t.%) until a homogeneous mixture was obtained. Subsequently, the mixture was sandwiched between quartz windows (Ø 12.7 mm, 3 mm thick) and the sample was mounted in a standard CD circular cell holder. Solid-state CD spectra were then recorded using a Jasco J-810 spectropolarimeter from 350 – 450 nm, using a resolution of 5 points/nm at a scan rate of 50 nm/min. The ε of unknown samples was calculated for all measured wavelengths, using linear interpolation of the recorded CD signal against known samples (100% *d*, 50% *d*, 0%, 50% *l*, 100% *l*). The homochiral crystals were prepared via a method similar to Kondepudi et al. [52] and the average ε value, estimated for all wavelengths was reported together with the standard deviation. The commercially available crystals of $NaClO_3$

(Sigma Aldrich) were found to have an initial ε of $\sim 20\%$ in favor of the *d* enantiomer. Further details on the ε estimation procedure are given in Supporting Information.

4. RESULTS

4.1 Breakage experiments using different methods of grinding

A first series of experiments was designed to investigate the particle size reduction of $NaClO_3$ crystals suspended in the nonsolvent hexane using three methods of grinding: a) bead grinding (40 g of glass beads), b) ultrasound grinding (41 kHz and 30 W) and c) the combination of both bead and ultrasound grinding. Figure 3 shows the experimental results in terms of the time evolution of the volume- and number-based PSDs for these experiments. As expected, in every case, particle size decreases in time, but the different experiments exhibit substantially different trends. When bead grinding is used (Figure 3, top row) a strong initial particle size reduction is obtained upon the first few minutes of grinding, (36 min), where the mean volume diameter ($D_{4,3}$) reached 31 μm from the initial value of 536 μm, followed by a more gradual decrease up to the final value of $D_{4,3}$ = 10.7 μm. Furthermore, the resulting PSD after 230 min is broader than the initial one and comprises mostly particles between roughly 1.5 – 50 μm. Ultrasonic treatment of the particles also results in particle size reduction (Figure 3, middle row), but contrary to bead grinding, a bimodal PSD is formed with a distinct separation between the primary particles and the finer fragment size modes. After 215 min of ultrasonication, the first mode consists of unbroken particles (90-1500 μm) having a $D_{4,3}$ almost equal to the initial one of 536 μm, while the second one is broader consisting of fine fragments (0.18-12 μm) with a $D_{4,3}$ of about 1.3 μm.

Another difference between bead and ultrasound grinding lies in formation of submicron fragments. When bead grinding is used, submicron fragments with a minimum size of circa 0.5

μm emerge only after prolonged grinding times (230 min, ~2% of total particle volume), with no such particles being observed at all during intermediate measurements. In contrast, using ultrasound grinding, smaller submicron particles (0.18-1 μm) start appearing already after 30 min of grinding and their amount keeps increasing throughout the grinding process, reaching about 30% of the total particle volume after 215 min. A higher fraction of submicron particles observed in the breakage experiments would also point out a faster generation of submicron particles for the counter enantiomer in an attrition-enhanced deracemization process. These submicron particles are more soluble that the larger crystals; for particle sizes of 0.18 - 1 μm the solubility is estimated at 0.13% - 0.70% higher (see Supporting Information) than the bulk solubility of $NaClO_3$ in water (~ 6.6 M). Thus, using ultrasound grinding, a higher fraction of the counter enantiomer is expected to dissolve and convert to the preferred enantiomer potentially leading to faster deracemization. For the bead grinding breakage experiment, the total mass of submicron particles formed in 230 min using bead grinding is about 400 mg, which for a racemic mixture, would give an average maximum mass of circa 0.87 mg/min of each enantiomer involved in the deracemization process. This value is in the same order of magnitude as the average mass conversion rate of the counter enantiomer to the preferred enantiomer observed in the original experiment of Viedma (0.83 mg/min) for $NaClO_3$ in water at similar conditions starting from the racemic mixture [1]. This observation may suggest that the actual size of fragments attained and their rate of formation is the rate limiting step in Viedma ripening using bead grinding, in particular for highly soluble compounds that racemize instantly or lose chiral identity when dissolved.

Figure 3 (bottom row) also shows the evolution of the PSD in time for a $NaClO_3$ breakage experiment using both bead and ultrasound grinding. The PSD evolution trend for that

experiment bears similarities to both previous cases where the two grinding methods were applied separately. Similar to the bead grinding experiment, a rapid initial particle breakage period is observed here as well (decrease in $D_{4,3}$ from 536 μm to 17.8 μm) in 35 min of grinding, followed by a more gradual decrease up to a final $D_{4,3}$ value of 5.3 μm. As expected though, the final particle size is smaller than bead grinding alone, due to the additional breakage supplied by the ultrasound. Similar to the ultrasound grinding experiment, submicron particles (0.33-1 μm) are again obtained directly after 35 min and their amount keeps increasing during the grinding process. At the end of the grinding experiment, these particles comprise about 9% of the total particle volume, a value in-between the two extremes obtained using bead grinding and ultrasound grinding individually, (2% and 30%, respectively).

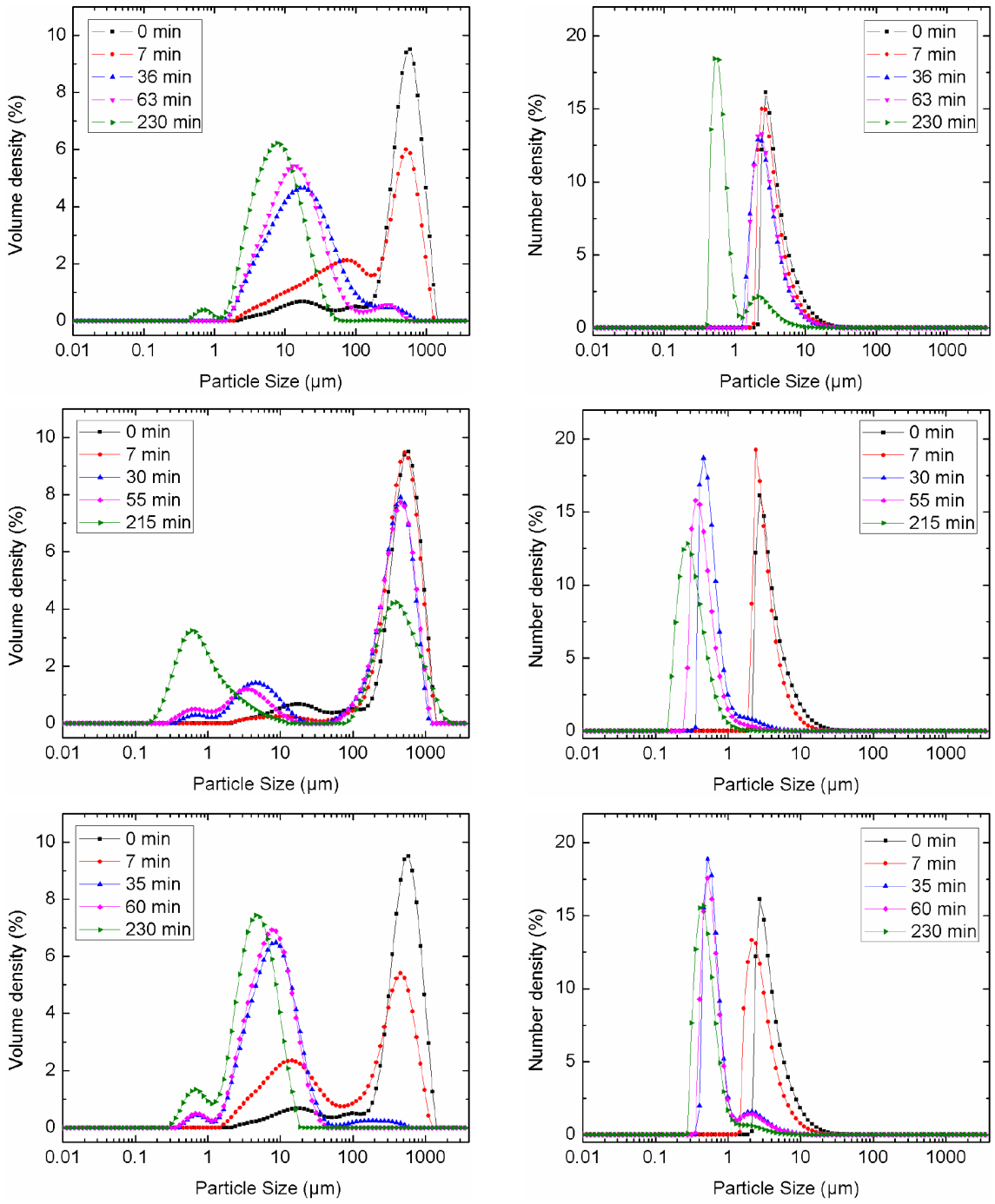

Figure 3. Evolution of the volume- (left column) and number-based (right column) particle size distributions (PSDs) in time, measured by laser diffraction, for $NaClO_3$ (20 g) breakage experiments in hexane for bead grinding using 40 g glass beads (top row), ultrasound at 41 kHz and 30W grinding (middle row) and the combination of the two methods (bottom row).

The results of the particle size analysis are confirmed by SEM images of the final product crystals, taken after the end of all grinding experiments as shown in Figure 4. Irregularly-shaped particles with surface defects and a broad PSD were obtained with bead grinding. Upon ultrasound grinding, a large amount of fine particles (< 10 μm) is found together with larger particles, closer to the initial sizes, confirming the bimodality of the PSD measured in Figure 3 (middle). Furthermore, a shape transition of the primary particles from cubes to spheres is obtained upon ultrasound grinding, indicative of particle abrasion. Indeed, this smoothening of the particles with ultrasound has been reported in the literature for both inorganic [53] and organic crystals [49] and is often attributed to abrasion caused by shockwaves and/or interparticle collisions [38]. Finally, in the combination of bead and ultrasound grinding, slightly smaller crystals with a narrower PSD are observed compared to the bead grinding, again confirming the results of the particle size analysis.

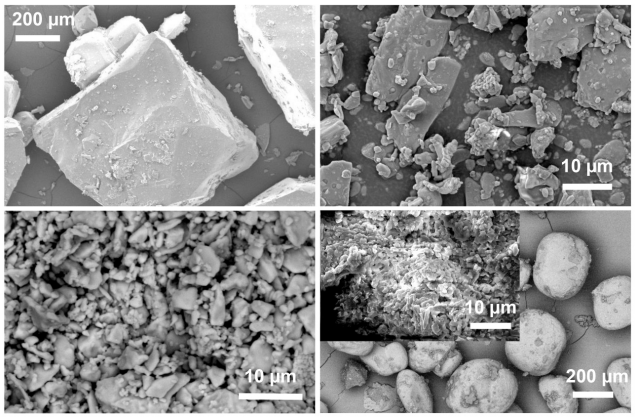

Figure 4. SEM pictures of, top left: the initial $NaClO_3$ crystals used in all breakage experiments, top right: final crystals after bead grinding alone, bottom right: final crystals after sonication alone, bottom left: final crystals after combination of bead grinding and sonication. Inset in bottom right picture shows the fine particles formed during the ultrasound breakage process.

4.2 Kinetic modeling of grinding and identification of breakage mechanisms

To gain more insight into the breakage mechanisms during grinding using beads and ultrasound, we performed kinetic modeling of the breakage process. The particle-size dependent breakage rates and the cumulative breakage distribution functions were derived for a) bead grinding, b) ultrasound grinding and c) the combination of the two methods, using the experimental data of Section 4.1. The kinetic modeling procedure is similar to the one described elsewhere [47–49] and the theory is explained in Section 2.

Firstly, the continuous PSD was discretized in 10 logarithmically-spaced particle size classes above 1 μm, as shown in Table 1. These size classes were selected in order to cover the entire range of particles above 1 μm, which are not expected to actively participate in a Viedma deracemization process. Note that the numbering of these size classes is done in reverse order with 1 corresponding to the coarsest class (> 100 μm) and 10 corresponding to the smallest size class considered (1.0 – 1.7 μm).

Next, based on the experimental PSD data series, the cumulative oversize fractions, $R_i(t)$ were calculated for each particle size class. Subsequently, the first Kapur function, $K_i^{(1)}$, was determined for every particle size class i by linear fits of $ln\left(\frac{R_i(t)}{R_i(0)}\right)$ to Eq. 4. For certain size classes, some of the later time data for $R_i(t)$ were excluded from the fit, in order to maintain $T <$ 95% according to Eq. 5, so that Eq. 4 is valid. The error in $K_i^{(1)}$ estimation was less than 15% in all cases. Finally, the approximate breakage rates, S_i and cumulative breakage distribution

functions, $B_{i,j}$ were calculated according to Eq. 6 and Eq. 7, respectively, for all size classes in Table 1.

Table 1. Definition of the particle size classes considered for the kinetic modeling of breakage.

Particle size class i, j	1	2	3	4	5	6	7	8	9	10
Particle size range (μm)	> 100	100 – 59.9	59.9 – 35.9	35.9 – 21.5	21.5 – 12.9	12.9 – 7.7	7.7 – 4.6	4.6 – 2.8	2.8 – 1.7	1.7 – 1.0

Figure 5 shows the breakage rate S_i as a function of the particle size for the different types of grinding considered in this study. The particle sizes reported in this figure correspond to the minimum size of each size class. It is seen that in all methods of grinding, the breakage rate increases with particle size, with a steep initial increase, but levels off as particle size increases further. The increase is less pronounced for ultrasound grinding, which shows the least dependence of the breakage rate on the particle size. A comparison between the different methods of grinding reveals that for particles > 7.7 μm, bead grinding is much more effective than ultrasound in breaking the crystals, with breakage rates up to an order of magnitude higher. However, for particles < 7.7 μm the trend is inverted and ultrasound becomes a more effective breakage mechanism. Indeed, size reduction of small particles has been reported to be challenging in stirred media mills mainly because the contact points of the particles with the beads decrease leading to a reduction in the stress frequency [40]. This effect can be circumvented by using a high loading of very small grinding media (in the μm range), at the expense, however, of reduced collision forces [40,54]. Hence, it appears that ultrasound grinding is a more suitable method for fine micro-grinding of smaller particles, where bead grinding is relatively ineffective.

The ultrasound breakage rates found here are also lower than those derived in a previous study for the sonofragmentation of paracetamol particles [49]. This means that while ultrasound grinding alone seems to be rather ineffective for reducing the size of the hard $NaClO_3$ crystals, it is likely that appreciable breakage rates are still attainable for more brittle organic crystals, such as those often involved in attrition-enhanced deracemization experiments.

Figure 5 also shows that the concomitant application of bead and ultrasound grinding affords the highest breakage rates, ~2 times higher on average than those found for bead grinding alone. Interestingly, for particles > 7.7 μm, a synergistic effect of bead and ultrasound grinding is observed. The origin of this effect is currently unknown, but some possible explanations can be hypothesized. Sonofragmentation of ionic crystals has been shown to occur mostly due to interactions of the particles with shockwaves and liquid microjets formed during the collapse of cavitation bubbles [38,41]. These interactions lead to breakage near cracks and defects present in crystals through compression-expansion and bending-torsion of the particles [41]. In the presence of additional impact forces due to the beads, cracks and defects are rapidly created on the larger particles and propagate radially outward from the point of impact creating fan-like structures [55]. Owing to the large number of cracks and defects created by the bead grinding, the crystals could progressively become more susceptible to ultrasound breakage compared to the initial crystals which would contain relatively fewer cracks and defects (Figure 4) [56]. Another possible explanation for the observed effect could be that microjets emanating from the implosion of cavitation bubbles in the vicinity of the beads can, to some extent, increase the velocity of the beads and therefore increase the magnitude of the applied stress on the particles upon impact.

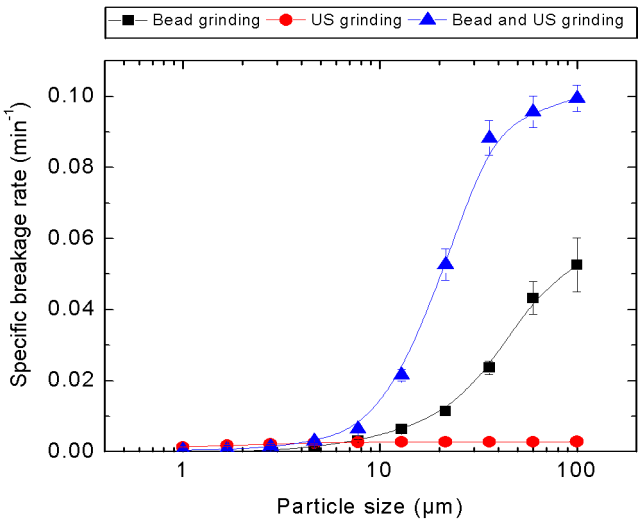

Figure 5. Breakage rate S_i as a function of particle size using bead grinding (black squares), ultrasound grinding (red circles) and the combination of the two methods (blue triangles). The particle size presented corresponds to the minimum particle size of each particle size class.

To identify the breakage mechanisms using the different grinding methods applied in this study, the cumulative breakage functions ($B_{i,j}$) were calculated for every size class and were plotted in Figure 6 against the relative particle size (x_i/x_j) for all grinding methods. The dashed curves in Figure 6 were taken from literature [51] and correspond to the two extreme cases, where breakage occurs either purely by fracture or abrasion. Figure 6 (top), shows that when bead grinding is applied, all experimental $B_{i,j}$ curves lie between the two extreme curves, but significantly closer to the fracture curve indicating that while both mechanisms are active in the breakage process, fracture is dominant. The effect is aggravated with decreasing particle size, where fracture becomes increasingly more dominant up until the $B_{i,j}$ curves almost coincide to the extreme curve for fracture. This observation is in accordance with literature reports for breakage in stirred media mills, wherein smaller particles have been reported to break mostly by fracture rather than abrasion [39]. Figure 6 (middle), shows that in the presence of ultrasound grinding, all $B_{i,j}$ curves

are again in-between the two extremes, but very close to the abrasion curve indicating that, contrary to bead grinding, abrasion is now the dominant breakage mechanism. For the largest size classes (> 59.9 μm), breakage occurs almost exclusively by abrasion, but as particle size decreases, fracture becomes increasingly important, similarly to the bead grinding, although unlike the latter case, abrasion remains the dominant breakage mechanism.

A mixed situation arises when ultrasound and bead grinding are combined (Figure 6, bottom). While the experimental $B_{i,j}$ curves for the combination of the two methods is closer to the fracture curve, indicating that fracture is dominant, relatively more abrasion is observed compared to the bead grinding method. This can be seen in a more clear manner also in Figure 7, where a comparison of only the $B_{i,1}$ curves is presented for all grinding methods. Similar to both previous methods, a shift towards fracture is obtained with decreasing particle size up to 21.5 μm, but when particle size decreases further, the trend is inverted and a shift towards abrasion starts to occur. This effect can be rationalized if one considers the competition between the different breakage mechanisms. Bead grinding provides strong impact forces leading to high breakage rates and fracture for the larger particles. It is thus reasonable to assume that even in the combination of ultrasound and bead grinding, it is the latter mechanism that will be responsible for most breakage of the larger crystals through fracture. However, as particle size becomes smaller (< 12.9 μm), bead grinding becomes significantly less effective and the breakage rates decrease to such extent that become comparable and even lower than the breakage rates attained with ultrasound (Figure 5). Thus, ultrasound starts to compete favorably for the breakage of these smaller crystals and since abrasion is dominant during sonofragmentation, a shift towards this region is observed.

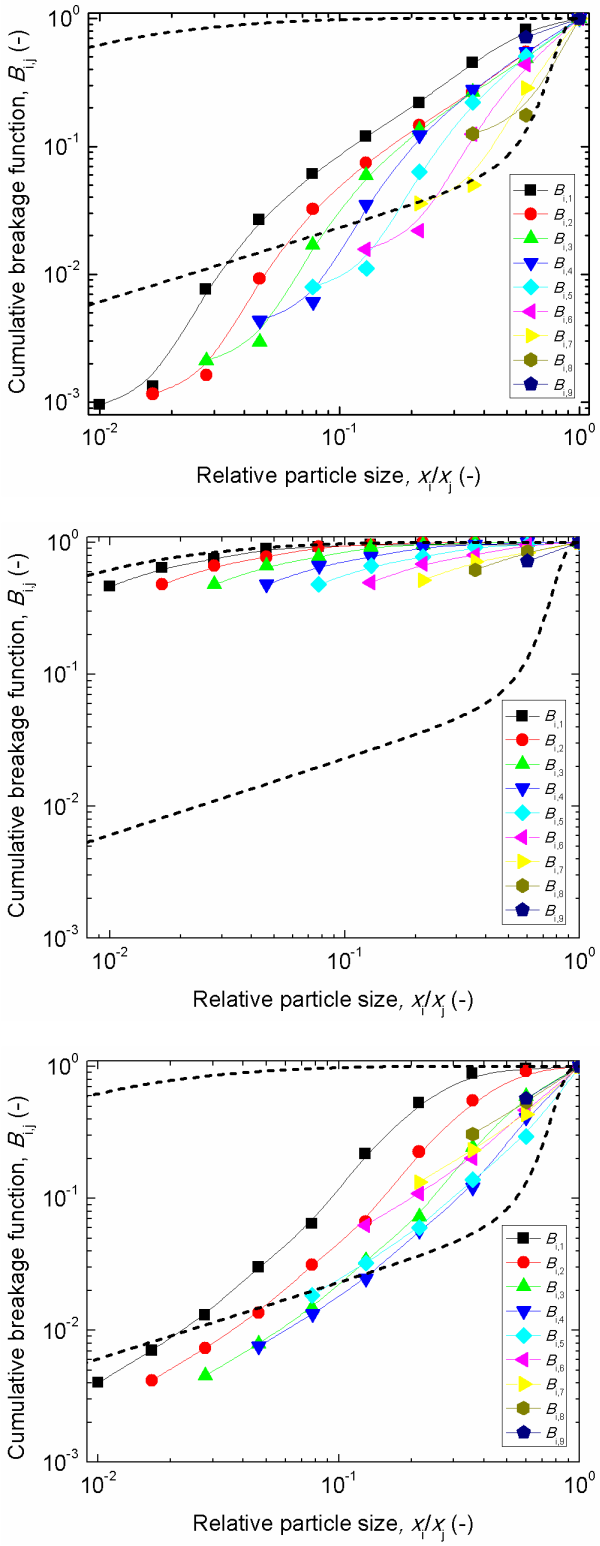

Figure 6. Cumulative breakage distribution functions, $B_{i,j}$, against relative particle size, x_i/x_j, for bead grinding (top), ultrasound grinding (middle) and the combination of the two methods

(bottom). The dashed curves correspond to $B_{i,1}$ curves for abrasion (upper curve) and fracture (lower curve) obtained from the literature [51].

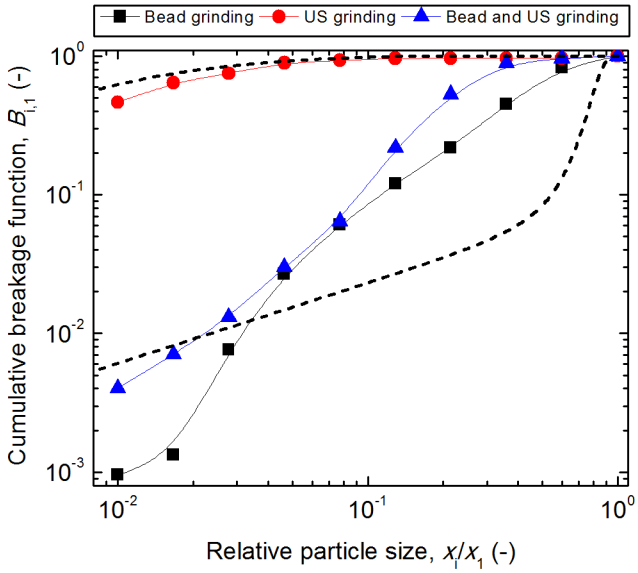

Figure 7. Cumulative breakage distribution functions for breakage of the top size class (> 100 µm), $B_{i,1}$, against relative particle size, x_i/x_1, for bead grinding (black squares), ultrasound grinding (red circles) and the combination of the two methods (blue triangles). The dashed curves correspond to $B_{i,1}$ curves for abrasion (upper curve) and fracture (lower curve) obtained from the literature [51].

4.3 Deracemization experiments using different methods of grinding

Although the analysis carried out in the previous sections gives important insights into the breakage mechanisms when different grinding methods are applied, our goal is to use these observations to understand the influence of the breakage mechanisms in a real attrition-enhanced deracemization process. To this end, we also carried out deracemization experiments using: a) bead grinding, b) ultrasound grinding and c) the combination of the two previous methods. All deracemization experiments were conducted in a saturated aqueous $NaClO_3$ solution using

otherwise same conditions as in our breakage experiments and the results in terms of the evolution of the solid phase enantiomeric excess (ε), monitored for 35 hours, are presented in Figure 8. In all cases, an initial steep increase in ε is observed, which is to some extent attributed to partial dissolution/recrystallization of the scalemic mixture when brought in contact with the saturated solution. The initial increase is steeper for the cases where ultrasound is applied, indicating that more deracemization occurs during this initial period for these cases. After this initial period, both bead grinding (black squares) and the combination of bead and ultrasound grinding (blue triangles) exhibit an exponential ε amplification, as reported in previous studies [1,34], with a decrease in the deracemization rate when ε approaches closer to 100%. Conversely, in ultrasound grinding alone ε levels off, similarly to our previous study, wherein ultrasound grinding led to fast but incomplete deracemization [36].

The results of the different deracemization experiments may be rationalized if one considers the different breakage mechanisms employed and their effects, as reported in sections 4.1 and 4.2. In the case of bead grinding, high breakage rates are attained (Figure 5), but breakage is dominated by fracture, giving a low probability for the generation of submicron fragments, which are essential for the deracemization process. Based on Figure 6 (top), the probability of submicron particle generation is estimated at: $B_{10,j}$= 0.1% – 3.6% for breakage of crystals between 100 – 4.6 μm, respectively. As particle size becomes smaller, this probability increases, but at the same time the breakage rates decrease dramatically, as seen in Figure 5. The end result is a slow generation of submicron fragments, visualized in Figure 3 (top), possibly leading to a slow rate of agglomeration for the enantiomer crystals in majority and dissolution for the enantiomer crystals in minority and subsequent slow deracemization. Conversely, in ultrasound grinding, abrasion dominates particle breakage, giving a very high probability for the generation of

submicron fragments from all size classes. According to Figure 6 (middle), this probability ranges between $B_{10,j}$= 46% – 52% for breakage of crystals between 100 – 4.6 μm, respectively. Consequently, ultrasound leads to fast production of fines, which subsequently agglomerate or (partially) dissolve and re-crystallize. Both mechanisms would lead to larger crystals and eventually to very fast initial deracemization. However, large crystals of both enantiomers are broken down much slower during sonication compared to bead grinding (Figure 5). During the deracemization process, these large crystals also grow faster than their smaller counterparts owing to their lower solubility. As a result, large crystals of the counter enantiomer also survive during the deracemization process and grow leading to levelling of ε as observed in Figure 8. This behavior bears some resemblance with results reported in computational studies for deracemization when low values of attrition rate are used [30,57].

Finally, when both grinding methods are combined, particle breakage still occurs mostly by fracture, but the contribution of ultrasound leads to relatively more abrasion. Hence, the probability for submicron particle generation slightly increases compared to the bead grinding case ($B_{10,j}$= 0.4% – 13% for crystals between 100 – 4.6 μm, respectively). In addition, the average breakage rate roughly doubles compared to bead grinding. As a result, the deracemization profile exhibits features from both ultrasound and bead grinding methods. The higher probability for submicron particle generation leads to a steeper initial ε increase. Additionally, doubling of the average breakage rate leads to approximately 2-fold higher deracemization rate.

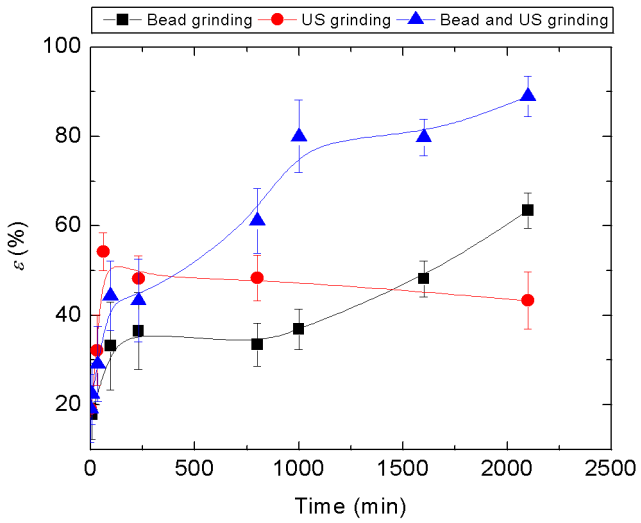

Figure 8. Attrition-enhanced deracemization experiments using bead grinding (black squares), ultrasound grinding (red circles) and the combination of the two methods (blue triangles). The lines serve as a guide to the eye (100% enantiomeric excess refers to pure *d*-$NaClO_3$ crystals).

5. DISCUSSION

As it is the case in most crystallization processes, including Viedma ripening, multiple mechanisms (growth-dissolution, breakage, agglomeration) affect the temporal evolution of PSD, which in turn affects the deracemization process itself. Since all mechanisms occur simultaneously during the deracemization process, it is generally difficult to experimentally isolate, study and optimize the effect of an individual mechanism (*e.g.* breakage). In this study, we propose an approach to isolate particle breakage effects in Viedma ripening processes by carrying out breakage experiments in nonsolvents, where there is no driving force for the additional phenomena to occur. Our results have shown that both breakage rate and mechanism substantially affect the deracemization process. Abrasion is a more desirable breakage mechanism as it minimizes the induction time before deracemization starts, although a

sufficiently fast breakage rate is also required to allow for the complete disappearance of most larger counter enantiomer crystals.

However, care should be exercised in transferring the results from nonsolvent breakage experiments to actual Viedma ripening experiments, as nonsolvents rarely have the same properties (*e.g.* density, viscosity) as the Viedma ripening solvents. This may lead to changes in the hydrodynamics between the two experiments that could eventually affect the grinding process. Yet, for small changes in the fluid properties, these effects are hardly important [40,41] and the qualitative nature of the grinding and its efficiency are not expected to change drastically. This means that even though the breakage rates attained in nonsolvent breakage experiments should be viewed mostly as an approximation to those in Viedma ripening experiments, they still allow for a relative comparison between different types of grinding and/or operating conditions [42]. For cases where the fluid properties change dramatically when moving to a nonsolvent from a Viedma ripening solvent, the use of additives to influence the solvent properties and achieve hydrodynamic similarity may also be considered.

Finally, it is worth mentioning that besides offering insight into the breakage process during Viedma ripening, the breakage kinetics derived here can be directly used in population balance models for Viedma ripening, such as the one proposed by Iggland and Mazzotti [30]. By coupling such data with experimentally derived growth/dissolution and agglomeration kinetics for a given compound, a quantitative model for Viedma ripening can be developed.

6. CONCLUSIONS

The results reported in this work help deconvolute the effect of particle breakage mechanism in attrition-enhanced deracemization process when different modes of grinding (beads, ultrasound)

are employed. It is shown that during the conventional bead grinding process, breakage occurs mostly by fracture. The size of the large crystals is rapidly reduced, but breakage rates become very low with decreasing particle size, leading to a rather slow formation of the more soluble submicron fragments. Consequently, only a small mass of the counter enantiomer crystals is involved in the deracemization process leading to relatively slow deracemization kinetics. Interestingly, the average mass production rate of submicron particles for each enantiomer is found to be in the same order of magnitude as the average mass conversion rate of the counter enantiomer to the preferred enantiomer, as observed in the original experiment of Viedma. This observation suggests that the rate of submicron particle formation is the rate limiting step in Viedma ripening processes using bead grinding. Contrary to bead grinding, ultrasound grinding leads to breakage by abrasion. Therefore, a large number of submicron particles are instantly formed leading to fast initial deracemization. However, in ultrasound grinding, larger crystals of the counter enantiomer are not sufficiently reduced in size, which allows them to survive and grow during the process leading to incomplete deracemization. The combination of bead and ultrasound grinding leads to increased abrasion compared to bead grinding alone, while fracture remains the dominant breakage mechanism. Remarkably, a synergistic effect is observed between ultrasound and bead grinding, which leads to a 2-fold higher average breakage rate than bead grinding alone, followed by a similar increase in the deracemization rate.

ASSOSIATED CONTENT

The Supporting Information is available free of charge on the ACS Publications website pubs.asc.org. Evaluation of particle breakage only due to the stirrer. Enantiomeric excess measurement procedure using solid-state circular dichroism (CD) and solid state spectra of

$NaClO_3$ crystals. Solution of the Gibbs-Thomson equation for $NaClO_3$ particles in aqueous solutions.

AUTHOR INFORMATION

Corresponding Author

* Email: Georgios.Stefanidis@cit.kuleuven.be

Author Contributions

The manuscript was written through contributions of all authors. All authors have given approval to the final version of the manuscript.

Notes

The authors declare no competing financial interest.

ACKNOWLEDGEMENT

C.X. acknowledges funding of a Ph.D. fellowship by the Research Foundation-Flanders (FWO). J.H.t.H. thanks the EPSRC Centre for Innovative Manufacturing in Continuous Manufacturing and Crystallization (http://www.cmac.ac.uk) for supporting this work (EPSRC funding under Grant Reference: EP/I033459/1). Professor Thierry Verbiest and Tom Swusten are thanked for providing their help with the CD measurements.

REFERENCES

(1) Viedma, C. Chiral symmetry breaking during crystallization: Complete chiral purity induced by nonlinear autocatalysis and recycling. *Phys. Rev. Lett.* **2005**, *94*, 3–6.

(2) Noorduin, W. L.; Izumi, T.; Millemaggi, A.; Leeman, M.; Meekes, H.; Van Enckevort, W. J. P.; Kellogg, R. M.; Kaptein, B.; Vlieg, E.; Blackmond, D. G. Emergence of a single solid chiral state from a nearly racemic amino acid derivative. *J. Am. Chem. Soc.* **2008**, *130*, 1158–1159.

(3) Noorduin, W. L.; Kaptein, B.; Meekes, H.; Van Enckevort, W. J. P.; Kellogg, R. M.; Vlieg, E. Fast attrition-enhanced deracemization of naproxen by a gradual in situ feed. *Angew. Chemie - Int. Ed.* **2009**, *48*, 4581–4583.

(4) Noorduin, W. L.; Van Der Asdonk, P.; Bode, A. A. C.; Meekes, H.; Van Enckevort, W. J. P.; Vlieg, E.; Kaptein, B.; Van Der Meijden, M. W.; Kellogg, R. M.; Deroover, G. Scaling up attrition-enhanced deracemization by use of an industrial bead mill in a route to clopidogrel (Plavix). *Org. Process Res. Dev.* **2010**, *14*, 908–911.

(5) Kellogg, R.; Van der Meijden, M.; Leeman, M.; Gelens, E.; Noorduin, W.; Meekes, H.; Van Enckevort, W.; Kaptein, B.; Vlieg, E. Attrition-enhanced deracemization in the synthesis of clopidogrel - a practical application of a new discovery. *Org. Process Res. Dev.* **2009**, *13*, 1195–1198.

(6) Viedma, C. Selective chiral symmetry breaking during crystallization: Parity violation or cryptochiral environment in control? *Cryst. Growth Des.* **2007**, *7*, 553–556.

(7) McLaughlin, D. T.; Nguyen, T. P. T.; Mengnjo, L.; Bian, C.; Leung, Y. H.; Goodfellow, E.; Ramrup, P.; Woo, S.; Cuccia, L. A. Viedma ripening of conglomerate crystals of achiral molecules monitored using solid-state circular dichroism. *Cryst. Growth Des.* **2014**, *14*, 1067–1076.

(8) Cheung, P. S. M.; Gagnon, J.; Surprenant, J.; Tao, Y.; Xu, H.; Cuccia, L. A. Complete asymmetric amplification of ethylenediammonium sulfate using an abrasion/grinding technique. *Chem. Commun.* **2008**, 8, 987–989.

(9) Wilmink, P.; Rougeot, C.; Wurst, K.; Sanselme, M.; Van Der Meijden, M.; Saletra, W.; Coquerel, G.; Kellogg, R. M. Attrition induced deracemisation of 2-fluorophenylglycine. *Org. Process Res. Dev.* **2015**, *19*, 302–308.

(10) Kaptein, B.; Noorduin, W. L.; Meekes, H.; Van Enckevort, W. J. P.; Kellogg, R. M.; Vlieg, E. Attrition-enhanced deracemization of an amino acid derivative that forms an epitaxial racemic conglomerate. *Angew. Chemie - Int. Ed.* **2008**, *47*, 7226–7229.

(11) Spix, L.; Alfring, A.; Meekes, H.; Van Enckevort, W. J. P.; Vlieg, E. Formation of a salt enables complete deracemization of a racemic compound through Viedma ripening. *Cryst. Growth Des.* **2014**, *14*, 1744–1748.

(12) Kawasaki, T.; Takamatsu, N.; Aiba, S.; Tokunaga, Y. Spontaneous formation and amplification of an enantioenriched α-amino nitrile: a chiral precursor for Strecker amino acid synthesis. *Chem. Commun.* **2015**, *51*, 14377–14380.

(13) Steendam, R. R. E.; Brouwer, M. C. T.; Huijs, E. M. E.; Kulka, M. W.; Meekes, H.; Van Enckevort, W. J. P.; Raap, J.; Rutjes, F. P. J. T.; Vlieg, E. Enantiopure isoindolinones through Viedma ripening. *Chem. - A Eur. J.* **2014**, *20*, 13527–13530.

(14) Engwerda, A. H. J.; Van Schayik, P.; Jagtenberg, H.; Meekes, H.; Rutjes, F. P. J. T.; Vlieg, E. Solid Phase deracemization of an atropisomer. *Cryst. Growth Des.* **2017**, 17, 5583–5585.

(15) Viedma, C.; Ortiz, J. E.; De Torres, T.; Izumi, T.; Blackmond, D. G. Evolution of solid phase homochirality for a proteinogenic amino acid. *J. Am. Chem. Soc.* **2008**, *130*, 15274–15275.

(16) Engwerda, A. H. J.; Koning, N.; Tinnemans, P.; Meekes, H.; Bickelhaupt, F. M.; Rutjes, F. P. J. T.; Vlieg, E. Deracemization of a racemic allylic sulfoxide using Viedma ripening. *Cryst. Growth Des.* **2017**, *17*, 4454–4457.

(17) Viedma, C.; Cintas, P. Homochirality beyond grinding: deracemizing chiral crystals by temperature gradient under boiling. *Chem. Commun.* **2011**, *47*, 12786.

(18) Suwannasang, K.; Flood, A. E.; Rougeot, C.; Coquerel, G. Using programmed heating-cooling cycles with racemization in solution for complete symmetry breaking of a conglomerate forming system. *Cryst. Growth Des.* **2013**, *13*, 3498–3504.

(19) Li, W. W.; Spix, L.; De Reus, S. C. A.; Meekes, H.; Kramer, H. J. M.; Vlieg, E.; Ter Horst, J. H. Deracemization of a racemic compound via its conglomerate-forming salt using temperature cycling. *Cryst. Growth Des.* **2016**, 16, 5563–5570.

(20) Steendam, R. R. E.; Verkade, J. M. M.; Van Benthem, T. J. B.; Meekes, H.; Van Enckevort, W. J. P.; Raap, J.; Rutjes, F. P. J. T.; Vlieg, E. Emergence of single-molecular chirality from achiral reactants. *Nat. Commun.* **2014**, *5*, 5543.

(21) Wei, S.; Mauksch, M.; Tsogoeva, S. B. Autocatalytic enantiomerisation at the crystal surface in deracemisation of scalemic conglomerates. *Chem. - A Eur. J.* **2009**, *15*, 10255–10262.

(22) Spix, L.; Meekes, H.; Blaauw, R. H.; Van Enckevort, W. J. P.; Vlieg, E. Complete deracemization of proteinogenic glutamic acid using Viedma ripening on a metastable conglomerate. *Cryst. Growth Des.* **2012**, *12*, 5796–5799.

(23) Xiouras, C.; Van Cleemput, E.; Kumpen, A.; Ter Horst, J. H.; Van Gerven, T.; Stefanidis, G. D. Towards deracemization in the absence of grinding through crystal transformation, ripening, and racemization. *Cryst. Growth Des.* **2016**, 17, 882–890.

(24) Engwerda, A. H. J.; Meekes, H.; Kaptein, B.; Rutjes, F. P. J. T.; Vlieg, E. Speeding up Viedma ripening. *Chem. Commun.* **2016**, *96*, 1659–1676.

(25) Steendam, R. R. E.; Dickhout, J.; Van Enckevort, W. J. P.; Meekes, H.; Raap, J.; Rutjes, F. P. J. T.; Vlieg, E. Linear deracemization kinetics during Viedma ripening: autocatalysis overruled by chiral additives. *Cryst. Growth Des.* **2015**, 15, 1975–1982.

(26) Nguyen, T. P. T.; Cheung, P. S. M.; Werber, L.; Gagnon, J.; Sivakumar, R.; Lennox, C.; Sossin, A.; Mastai, Y.; Cuccia, L. A. Directing the Viedma ripening of ethylenediammonium sulfate using “tailor-made” chiral additives. *Chem. Commun.* **2016**, *52*, 12626–12629.

(27) Uwaha, M. *J.* A model for complete chiral crystallization. *Phys. Soc. Japan* **2004**, *73*, 2601–2603.

(28) McBride, J. M.; Tully, J. C. Did life grind to a start? *Nature* **2008**, *452*, 161–162.

(29) Noorduin, W. L.; Van Enckevort, W. J. P.; Meekes, H.; Kaptein, B.; Kellogg, R. M.; Tully, J. C.; McBride, J. M.; Vlieg, E. The driving mechanism behind attrition-enhanced deracemization. *Angew. Chemie - Int. Ed.* **2010**, *49*, 8435–8438.

(30) Iggland, M.; Mazzotti, M. A population balance model for chiral resolution via Viedma ripening. *Cryst. Growth Des.* **2011**, *11*, 4611–4622.

(31) Hein, J. E.; Huynh Cao, B.; Viedma, C.; Kellogg, R. M.; Blackmond, D. G. Pasteur's Tweezers revisited: On the mechanism of attrition-enhanced deracemization and resolution of chiral conglomerate solids. *J. Am. Chem. Soc.* **2012**, *134*, 12629–12636.

(32) Mersmann, A. *Crystallization Technology Handbook*; 1995; Vol. 13.

(33) Xiouras, C.; Fytopoulos, A.; Jordens, J.; Boudouvis, A. G.; Gerven, T. Van; Stefanidis, G. D. Applications of ultrasound to chiral crystallization, resolution and deracemization. *Ultrason. Sonochem.* **2018**, *43*, 184–192.

(34) Noorduin, W. L.; Meekes, H.; Van Enckevort, W. J. P.; Millemaggi, A.; Leeman, M.; Kaptein, B.; Kellogg, R. M.; Vlieg, E. Complete deracemization by attrition-enhanced Ostwald ripening elucidated. *Angew. Chemie - Int. Ed.* **2008**, *47*, 6445–6447.

(35) Steendam, R. R. E.; Harmsen, B.; Meekes, H.; Van Enckevort, W. J. P.; Kaptein, B.; Kellogg, R. M.; Raap, J.; Rutjes, F. P. J. T.; Vlieg, E. Controlling the effect of chiral impurities on Viedma ripening. *Cryst. Growth Des.* **2013**, *13*, 4776–4780.

(36) Xiouras, C.; Van Aeken, J.; Panis, J.; Ter Horst, J. H.; Van Gerven, T.; Stefanidis, G. D. Attrition-enhanced deracemization of NaClO3: Comparison between ultrasonic and abrasive grinding. *Cryst. Growth Des.* **2015**, 15, 5476–5484.

(37) Rougeot, C.; Guillen, F.; Plaquevent, J.-C.; Coquerel, G. Ultrasound-enhanced deracemization: Toward the existence of agonist effects in the interpretation of spontaneous symmetry breaking. *Cryst. Growth Des.* **2015**, 15, 2151–2155.

(38) Sander, J. R. G.; Zeiger, B. W.; Suslick, K. S. Sonocrystallization and sonofragmentation. *Ultrason. Sonochem.* **2014**, *21*, 1908–1915.

(39) Hennart, S. L. A.; Wildeboer, W. J.; Van Hee, P.; Meesters, G. M. H. Identification of the grinding mechanisms and their origin in a stirred ball mill using population balances. *Chem. Eng. Sci.* **2009**, *64*, 4123–4130.

(40) Kwade, A.; Schwedes, J. Chapter 6: Wet Grinding in Stirred Media Mills. In *Particle Breakage*; Elsevier Science B.V., **2007**, 12, 251–382.

(41) Kim, H. N.; Suslick, K. S. Sonofragmentation of ionic Crystals. *Chem. - A Eur. J.* **2017**, *23*, 2778–2782.

(42) Reeves, S. M.; Hill, P. J. Mechanisms influencing crystal breakage experiments in stirred vessels. *Cryst. Growth Des.* **2012**, *12*, 2748–2758.

(43) Austin, L. G. Introduction to the mathematical description of grinding as a rate process. *Powder Technol*. **1971**, *5*, 1–17.

(44) Kapur, P. C.; Agrawal, P. K. Approximate solutions to the discretized batch grinding equation. *Chem*. *Eng*. *Sci*. **1970,** 25, 1111-1113.

(45) Berthiaux, H.; Varinot, C.; Dodds, J. Approximate calculation of breakage parameters from batch grinding tests. *Chem*. *Eng*. *Sci*. **1996**, *51*, 4509–4516.

(46) Kapur, P. C. An improved method for estimating the feed-size breakage distribution functions. *Powder Technol*. **1982**, *33*, 269–275.

(47) Varinot, C.; Hiltgun, S.; Pons, M. N.; Dodds, J. Identification of the fragmentation mechanisms in wet-phase fine grinding in a stirred bead mill. *Chem*. *Eng*. *Sci*. **1997**, *52*, 3605–3612.

(48) Raman, V.; Abbas, A.; Zhu, W. Particle grinding by high-intensity ultrasound: Kinetic modeling and identification of breakage mechanisms. *AIChE J*. **2011**, *57*, 2025–2035.

(49) Jordens, J.; Appermont, T.; Gielen, B.; Van Gerven, T.; Braeken, L. Sonofragmentation: Effect of ultrasound frequency and power on particle breakage. *Cryst*. *Growth Des*. **2016**, *16*, 6167–6177.

(50) Kelly, E. G.; Spottiswood, D. J. The breakage function; what is it really? *Mineral Eng*. **1990**, *3*, 405–414.

(51) Menacho, J. M. Some solutions for the kinetics of combined fracture and abrasion breakage. *Powder Technol*. **1986**, *49*, 87–95.

(52) Kondepudi, D. K. K.; Kaufman, R. J. J.; Singh, N. Chiral symmetry breaking in sodium chlorate crystallisation. *Science* **1990**, *250*, 975–976.

(53) Suslick, K. S.; Price, G. J. Application of ultrasound to materials chemistry. *Annu*. *Rev*. *Mater*. *Sci* **1999**, *29*, 295–326.

(54) Yokoyama, T.; Inoue, Y. Chapter 10: Selection of fine grinding mills. In *Particle Breakage*; Elsevier Science B.V., **2007**, *12*, 487–508.

(55) Potapov, A. V.; Campbell, C. S. The two mechanisms of particle impact breakage and the velocity effect. *Powder Technol*. **1997**, *93*, 13–21.

(56) Teipel, U.; Leisinger, K.; Mikonsaari, I. Comminution of crystalline material by ultrasonics. *Int*. *J*. *Miner*. *Process*. **2004**, *74*, 183–190.

(57) Xiouras, C.; Ter Horst, J. H.; Van Gerven, T.; Stefanidis, G. D. Coupling Viedma ripening with racemic crystal transformations: Mechanism of deracemization. *Cryst*. *Growth Des*. **2017**, *17*, 4965–4976.

For Table of Contents Use Only

Particle Breakage Kinetics and Mechanisms in Attrition-Enhanced Deracemization

Christos Xiouras, Antonios A. Fytopoulos,, Joop H. Ter Horst, Andreas G. Boudouvis, Tom Van Gerven and Georgios D. Stefanidis

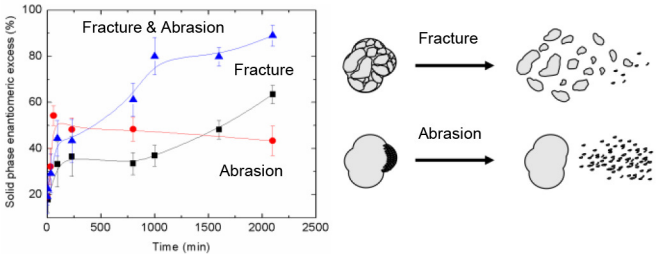

Through decoupling experiments and a mathematical model for breakage processes, we derive the specific breakage rates and cumulative distribution functions for different grinding methods typically used in deracemization experiments (bead/ultrasound grinding). We show that while abrasion is more desirable for deracemization, fracture rates should also be high enough to allow for sufficient size reduction of large counter enantiomer crystals.